# Shaping MOF Oxime Oxidation Catalysts as Three-dimensional Porous Aerogels through Structure-Directing Growth Inside of Chitosan Microspheres

Nirine Hammi, [a,b,c] Shuo Chen,[c] Ana Primo,[b] Sebastien Royer,[c] Hermenegildo Garcia,[b,*]Abdelkrim El Kadib,[a,*]

a. *Euromed Research Center, Engineering Division, Euro-Med University of Fes (UEMF), Route de Meknes, Rond-point de Bensouda, 30070, Fès, Morocco. Corresponding author: a.elkadib@ueuromed.org*
b. *Instituto de Tecnología Química (CSIC-UPV) and Departamento de Química (UPV), Universitat Politècnica de València, Av. de los Naranjos s/n, 46022 Valencia, Spain.*
c. *Univ. Lille, CNRS, Centrale Lille, ENSCL, Univ. Artois, UMR 8181 - UCCS - Unité de Catalyse et Chimie du Solide, F-59000 Lille, France.*

## S1. General bibliography and experimental section

**Table S1.** Overview of MOF based aerogels.

| Aerogel name | Matrix, additives | MOF | Synthesis method | Drying technique | MOF Loading, wt.% | MOF size, nm | $S_{BET}$, $m^2/g$ | $D_p$, nm | $V_p$, $cm^3/g$ | Shape | Use | ref |
|---|---|---|---|---|---|---|---|---|---|---|---|---|
| Ru/graphene aerogel-HKUST-1 | Ru/graphene aerogel, silane, succinic anhydride | HKUST-1 | In situ | freeze drying | 30 | 100-300 | 104 | - | - | monolith | CO oxidation | [1] |
| HKUST-1@silica aerogel | silica sol | HKUST-1 | Direct mixing | supercritical CO2 drying | 30 | - | - | - | - | monolith | styrene oxide isomerization | [2] |
| Fe-bpdc-C3N4-carbon aerogel | g-C3N4, resorcinol-formaldehyde | Fe-bpdc | Direct mixing | air drying | - | - | 440 | - | - | powder (ball-milled) | oxygen reduction reaction (ORR) | [3] |
| MOF(2Fe/Co)/carbon aerogel | carbon aerogel | MOF(Fe/Co) | In situ | ambient pressure drying | - | - | - | - | - | monolith | solar photo–electro–Fenton process | [4] |
| ZIF-9/cellulose aerogel | cellulose aerogel | ZIF-9 | In situ | freeze drying | 38 | 400 | 401 | 2,0 | 1,4 | monolith | p-nitrophenol degradetion | [5] |
| ZIF-12/cellulose aerogel | cellulose aerogel | ZIF-12 | In situ | freeze drying | 31 | - | 75 | 3,9 | 0,5 | monolith | p-nitrophenol degradetion | [5] |
| ZIF-8@rGO aerogels | GO nanosheet, hydrazine hydrate | ZIF-8 | In situ | freeze drying | - | 100 | 168 | - | - | monolith | photocatalytic degradation of methyl blue | [6] |
| ZIF-8/agar aerogel | agar aerogel, C3N4 nanosheet | ZIF-8 | In situ | freeze drying | 50 | 15 | - | - | - | monolith | Photocatalytic removal of Congo Red and Methylene Blue | [7] |
| HKUST-1/ polyacrylamides | polyacrylamides, Fe3O4, Triton X-405 | HKUST-1 | In situ | air drying at 60 °C | 54 | 4 μm | 701 | - | 0,34 | monolith | isomerization of α-pinene oxide | [8] |
| MOF-2 / polyacrylamides | polyacrylamides, Fe3O4, Triton X-405 | MOF-2 | In situ | air drying at 60 °C | 23,8 | 5 μm | 68 | - | - | monolith | isomerization of α-pinene oxide | [8] |
| UiO-66 / polyacrylamides | polyacrylamides, Fe3O4, Triton X-405 | UiO-66 | In situ | air drying at 60 °C | 17,6 | 30-100 | 202 | - | - | monolith | isomerization of α-pinene oxide | [8] |
| Fe-MIL-101(-NH2) / polyacrylamides | polyacrylamides, Fe3O4, Triton X-405 | Fe-MIL-101(-NH2) | In situ | air drying at 60 °C | 17.3 | - | 522 | - | - | monolith | isomerization of α-pinene oxide | [8] |

| | | | | | | | | | | | | |
|---|---|---|---|---|---|---|---|---|---|---|---|---|
| ZIF-8/rGO | graphene oxide, ascorbic acid, NaOH | ZIF-8 | In situ | freeze drying | - | - | 1341 | 2; 10 | - | monolith | cellulose degradation | [9] |
| ZIF-8@wood aerogel | wood aerogel | ZIF-8 | In situ | freeze drying | 75 | - | ~800 | 2; 14 | - | monolith | Knoevenagel reaction | [10] |
| CuBDC/ Carboxymethylcellulose | carboxymethyl cellulose | CuBDC | In situ | freeze drying | 10,5 | 0,1 μm | - | 0,65 | - | monolith | CO2 cycloaddition and oxygen evolution reaction | [11] |
| UiO-66/ cellulose aerogel | TEMPO-oxidized cellulose nanofibers, ZrCl4 crosslink | UiO-66 | Direct mixing | freeze drying | 54 | 108 | 483 | - | 0,23 | monolith | methyl paraoxon hydrolysis | [12] |
| UiO-66-NH2/ polyimide polymers | polyimide monomer (4,4'-oxydianiline), | UiO-66-NH2 | Direct mixing | freeze drying | 20 | - | - | 0,65 | - | monolith | CO2 cycloaddition | [13] |
| Alginate@MIL-101@Fe3O4 | calcium alginate, Fe3O4 nanoparticles | MIL-101 | Direct mixing | freeze drying | - | - | - | - | - | beads | reduction of dyes | [14] |


[1] J. Qu, D. Chen, N. Li, Q. Xu, H. Li, J. He, J. Lu, Engineering 3D Ru/Graphene Aerogel Using Metal–Organic Frameworks: Capture and Highly Efficient Catalytic CO Oxidation at Room Temperature, Small. 14 (2018) 1800343. https://doi.org/10.1002/smll.201800343.

[2] A.S. Shalygin, A.L. Nuzhdin, G.A. Bukhtiyarova, O.N. Martyanov, Preparation of HKUST-1@silica aerogel composite for continuous flow catalysis, J Sol-Gel Sci Technol. 84 (2017) 446–452. https://doi.org/10.1007/s10971-017-4455-3.

[3] H. Zhu, M. Chen, K. Li, X. Huang, F. Wang, Composite Electrocatalyst Derived from Hybrid Nitrogen-Containing Metal Organic Frameworks and g-C3N4 Encapsulated In Situ into Porous Carbon Aerogels, ChemElectroChem. 5 (2018) 2126–2134. https://doi.org/10.1002/celc.201800479.

[4] H. Zhao, Y. Chen, Q. Peng, Q. Wang, G. Zhao, Catalytic activity of MOF(2Fe/Co)/carbon aerogel for improving H2O2 and OH generation in solar photo–electro–Fenton process, Applied Catalysis B: Environmental. 203 (2017) 127–137. https://doi.org/10.1016/j.apcatb.2016.09.074.

[5] W. Ren, J. Gao, C. Lei, Y. Xie, Y. Cai, Q. Ni, J. Yao, Recyclable metal-organic framework/cellulose aerogels for activating peroxymonosulfate to degrade organic pollutants, Chemical Engineering Journal. 349 (2018) 766–774. https://doi.org/10.1016/j.cej.2018.05.143.

[6] J. Mao, M. Ge, J. Huang, Y. Lai, C. Lin, K. Zhang, K. Meng, Y. Tang, Constructing multifunctional MOF@rGO hydro-/aerogels by the self-assembly process for customized water remediation, J. Mater. Chem. A. 5 (2017) 11873–11881. https://doi.org/10.1039/C7TA01343D.

[7] W. Zhang, S. Shi, W. Zhu, L. Huang, C. Yang, S. Li, X. Liu, R. Wang, N. Hu, Y. Suo, Z. Li, J. Wang, Agar Aerogel Containing Small-Sized Zeolitic Imidazolate Framework Loaded Carbon Nitride: A Solar-Triggered Regenerable Decontaminant for Convenient and Enhanced Water Purification, ACS Sustainable Chem. Eng. 5 (2017) 9347–9354. https://doi.org/10.1021/acssuschemeng.7b02376.

[8] L. Chen, X. Ding, J. Huo, S. El Hankari, D. Bradshaw, Facile synthesis of magnetic macroporous polymer/MOF composites as separable catalysts, J Mater Sci. 54 (2019) 370–382. https://doi.org/10.1007/s10853-018-2835-x.

[9] P. Huang, L. Yan, Efficient Degradation of Cellulose in Its Homogeneously Aqueous Solution over 3D Metal-Organic Framework/Graphene Hydrogel Catalyst, Chinese Journal of Chemical Physics. 29 (2016) 742–748. https://doi.org/10.1063/1674-0068/29/cjcp1604073.

[10] M.-B. Wu, C. Zhang, Y. Xie, S. Huang, C. Liu, J. Wu, Z.-K. Xu, Janus Metal–Organic Frameworks/Wood Aerogel Composites for Boosting Catalytic Performance by Le Châtelier's Principle, ACS Appl. Mater. Interfaces. 13 (2021) 51039–51047. https://doi.org/10.1021/acsami.1c15738.

[11] X.-J. Bai, X.-Y. Lu, R. Ju, H. Chen, L. Shao, X. Zhai, Y.-N. Li, F.-Q. Fan, Y. Fu, W. Qi, Preparation of MOF Film/Aerogel Composite Catalysts via Substrate-Seeding Secondary-Growth for the Oxygen Evolution Reaction and CO2 Cycloaddition, Angewandte Chemie. 133 (2021) 711–715. https://doi.org/10.1002/ange.202012354.

[12] J.Y. Seo, Y. Song, J.-H. Lee, H. Kim, S. Cho, K.-Y. Baek, Robust Nanocellulose/Metal–Organic Framework Aerogel Composites: Superior Performance for Static and Continuous Disposal of Chemical Warfare Agent Simulants, ACS Appl. Mater. Interfaces. 13 (2021) 33516–33523. https://doi.org/10.1021/acsami.1c08138.
[13] Y. Xu, X. Zhai, X.-H. Wang, L.-L. Li, H. Chen, F.-Q. Fan, X.-J. Bai, J.-Y. Chen, Y. Fu, Fabrication of a robust MOF/aerogel composite via a covalent post-assembly method, Chem. Commun. 57 (2021) 5961–5964. https://doi.org/10.1039/D1CC01613J.
[14] M. Hachemaoui, A. Mokhtar, S. Abdelkrim, R. Ouargli-Saker, F. Zaoui, R. Hamacha, H. H. Zahmani, S. Hacini, A. Bengueddach, B. Boukoussa, Improved Catalytic Activity of Composite Beads Calcium Alginate@MIL-101@Fe3O4 Towards Reduction Toxic Organic Dyes, J Polym. Environ. 29 (2021) 3813–3826. https://doi.org/10.1007/s10924-021-02177-4

**Table S2.** Overview of the catalyst samples tested in the oxime's oxidation.

| Reagent | Catalyst | Oxidizing reagent | Solvent | P (bar) | T (°C) | Conv. (%) | Yield (%) | Remark | Ref. |
|---|---|---|---|---|---|---|---|---|---|
| Cyclohexanone oxime | Amberlite IRA-400 supported chromic acid in the presence of ZrCl4 (PCrO4H-ZrCl4) | | H2O, CH3CN | - | Reflux | 96 | | The use of Acid | [1] |
| | [C5H5N+ (CH2)14CH3]3{PO4[WO(O2)2]4}3– (PCWP) | H2O2 | H2O/CHCl3 | - | 30 | 90 | 90 | - | [2] |
| | Titanium silica-l(TS-1) | H2O2 | Acetone | - | Reflux | | 75 | The by-product of hydrogen peroxide is water, it is always more advantageous to use oxygen instead of H2O2 as an oxidizing reagent. | [3] |
| | Au (0.72 wt.%)/CeO2 | oxygen | EtOH/H2O | 5 | 130 | 99 | 99 | The use of oxidizing reagents that do not generate wastes | [4] |
| | Double metal hexacyanocobaltate (Mn2+, Co2+, Ni2+ and Cu2+) | oxygen | EtOH/H2O | 5 | 100 | 94 | 82 | Limitations of the oxidation with oxygen are the high activation barriers and poor selectivity The use of a catalyst which is able to decrease the activation energies and direct the process toward a single product. | [5] |
| | Amberlyst-15 and NaNO2 | oxygen | CH3CN/H2O | purged several times | 25 | | 82 | - | [6] |
| | FPA53 containing nitrite functional group resin (FPA53-NO2) and Amberlyst-15 | oxygen | - | 1 | 60 | | 19 | - | [7] |
| | Ce(SO4)2 | Ce(SO4)2 | chloroform | - | 25 | | 65 | - | [8] |
| | CrO2 | CrO2 | MeCN | - | 80 | | 18 | - | [9] |
| | SnCl2/TiCl3 and hydrochloric acid | | THF/H2O | - | 25 | | 91 | - | [10] |
| | (PhCH2Se)2 | H2O2 | Petroleum ether | - | 60 | | 99 | - | [11] |

[1] K. BAHRAMI, M.-M. KHODAEI, U. G. KARAJI, Transformation of Oximes and Alcohols to Carbonyl Compounds Using Amberlite IRA-400 Supported Chromic Acid in the Presence of Zirconium Tetrachloride, Chin. J. Chem. 27 (2009) 384-388. https://doi.org/10.1002/cjoc.200990063.
[2] F.P. Ballistreri, U. Chiacchio, A. Rescifina, G. Tomaselli, R.M. Toscano, Conversion of Oximes to Carbonyl Compounds by Triscetylpyridinium Tetrakis(oxodiperoxotungsto) Phosphate (PCWP)-mediated Oxidation with Hydrogen Peroxide, Molecules. 13 (2008) 1230-1237. https://doi.org/10.3390/molecules13061230
[3] R. Joseph, A. Sudalai, T. Ravindranathan, Selective catalytic oxidative cleavage of oximes to carbonyl compounds with H2O2 over TS-1, Tetrahedron Letters. 35 (1994) 5493-5496. https://doi.org/10.1016/S0040-4039(00)73533-7
[4] A. Grirrane, A. Corma, H. Garcia, Gold nanoparticles supported on ceria promote the selective oxidation of oximes into the corresponding carbonylic compounds, Journal of Catalysis. 268 (2009) 350-355. https://doi.org/10.1016/j.jcat.2009.10.005
[5] A. García-Ortiz, A. Grirrane, E. Reguera, H. García, Mixed (Fe2+ and Cu2+) double metal hexacyanocobaltates as solid catalyst for the aerobic oxidation of oximes to carbonyl compounds, Journal of Catalysis. 311 (2014) 386-392. https://doi.org/10.1016/j.jcat.2013.12.011
[6] G. Zhang, X. Wen, Y. Wang, W. Mo, C. Ding, Sodium Nitrite Catalyzed Aerobic Oxidative Deoximation under Mild Conditions, The Journal of Organic Chemistry. 76 (2011) 4665-4668. https://doi.org/10.1021/jo102571e
[7] S. Guo, R. Zeng, C. Li, Nitrite-containing resin as an efficient and recyclable catalyst for aerobic oxidation of oximes to carbonyl compounds, Synthetic Communications. 46 (2016) 1446-1453. https://doi.org/10.1080/00397911.2016.1211290
[8] O. Asutay, N. Hamarat, N. Uludag, N. Coşkun, Selective oxidative deoximation with anhydrous Ce(IV) sulfate, Tetrahedron Letters. 56 (2015) 3902-3904. https://doi.org/10.1016/j.tetlet.2015.04.111
[9] S. Bhosale, D. P. Sonune, U. V. Prasad, D. Bhuniya, Inverse kinetic isotope effect in Magtrieve™ mediated oxidation or deoximation of benzaldoxime: mechanistic implication, Tetrahedron Letters. 53 (2012) 1794-1797. https://doi.org/10.1016/j.tetlet.2012.01.111
[10] M.-H. Lin, H. -J. Liu, C.-Y. Chang, W. -C. Lin, T. -H. Chuang, SnCl2/TiCl3-Mediated Deoximation of Oximes in an Aqueous Solvent, Molecules. 17 (2012) 2464-2473. https://doi.org/10.3390/molecules17032464
[11] X. Jing, D. Yuan, L. Yu, Green and Practical Oxidative Deoximation of Oximes to Ketones or Aldehydes with Hydrogen Peroxide/Air by Organoselenium Catalysis, Adv. Synth. Catal. 359 (2017) 1194. https://doi.org/10.1002/adsc.201601353

**Characterization techniques**

$N_2$-physisorption isotherms were recorded at -196 °C on a Micromeritics Tristar II automated gas sorption system. Before analysis, the samples were outgassed under dynamic vacuum at 120 °C overnight. Specific surface area was determined using the multipoint B.E.T. algorithm in the $P/P_0$ range from 0.1 to 0.25 and the total pore volume is determined on the adsorption branch at $P/P_0 = 0.98$. The pore diameters and the pore size distributions were calculated from the desorption branch using the Barrett–Joyner–Halenda (BJH) and Non local density functional theory (NLDFT) methods. A Micromeritics Autopore IV 9500 penetrometer was used to investigate the mercury intrusion porosimetry of the samples, and a contact angle of 130° was assumed in the pore size calculations. X-ray diffraction (XRD) was performed using a Bruker X-ray AXS D8 Advance diffractometer in Bragg-Brentano configuration and equipped with a LynxEye Super Speed detector. XRD patterns were recorded with Cu Kα radiation (λ = 0.154 nm, 40 kV, 30 mA) in the 10–80° 2θ range with a 0.02° 2θ step. Phase identification was made by comparison with the ICDD database. Transmission electron microscopy (TEM) images were taken on a Philips CM 300 FEG system with an operating voltage of 100 kV. The sample to be analyzed was prepared using a microtoming technique with a focused ion beam. Diffuse reflectance infrared Fourier transform (DRIFT) spectra were monitored using a NICOLET iS10 spectrometer. A KRATOS Axis Ultra spectrometer operated under ultrahigh vacuum condition, using a twin Al X-ray source (1486.6 eV) at a pass energy of 40 eV, was used for the X-ray photoelectron spectroscopy (XPS) analyses. The solid, in the form of pellet, was fixed on a copper holder with copper tape. The binding energy values were estimated, positioning the C 1s peak of contaminant carbon at a B.E. of 285.0 eV. The Casa XPS software package was used for data analysis. TGA profiles were obtained on TGA SDT2960 under the constant flow of simulated air in the room temperature-900°C range with a 5°C/min rate. A Vinci Technologies Versatile Crushing Strength Tester was used to perform the single-particle crushing test, using a set of flat anvil and hammer. The load applied was recorded by the force sensor as a function of the displacement of the punch at a constant speed of 0.6 mm/min until failure, happening at the ultimate crushing strength of the solid. For each sample, 10 representative solids were crushed and the resulting crushing strength values, given in Newton, were averaged. .

**Table S3.** The specific experimental conditions.

| Sample code | Metal precursors | Molar ratio $NH_2$:metal precursor | Ligand | Synthesis T(°C) |
|---|---|---|---|---|
| **HKUST-1@CS** | $Cu(NO_3)_2 \cdot 2.5H_2O$ | 1:2 | BTC | 80 |
| **ZIF-67@CS** | $Co(NO_3)_2 \cdot 6H_2O$ | 1:2 | 2-Methylimidazole | 80 |
| **ZIF-8@CS** | $Zn(NO_3)_2 \cdot 6H_2O$, | 1:2 | 2-Methylimidazole | 40 |
| **Fe-BTC@CS** | $Fe(NO_3)_3 \cdot 9H_2O$ | 1:2 | BTC | 120 |

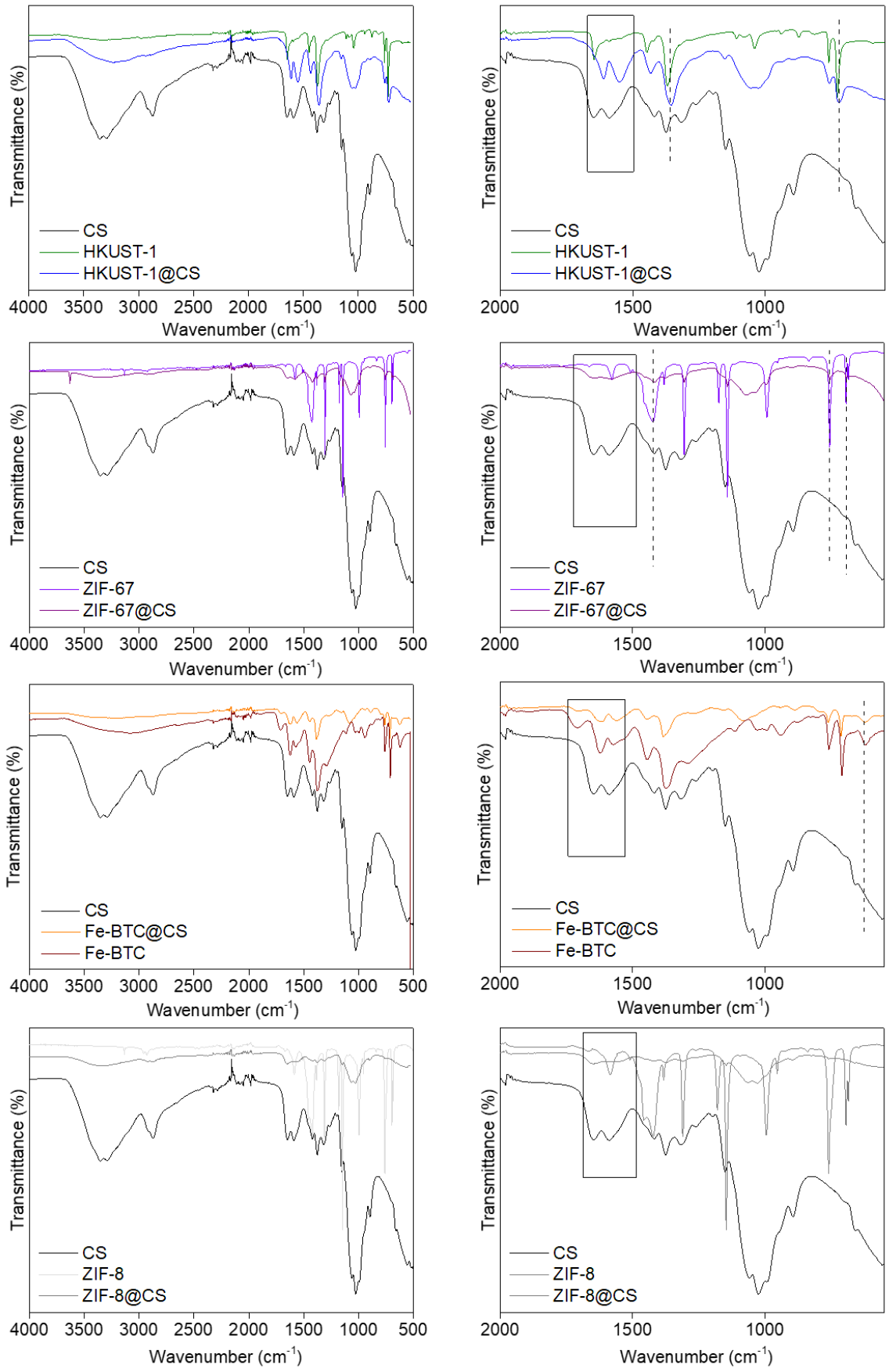


**Figure S1.** FTIR spectra of chitosan pristine, MOF and MOF@chitosan composite.

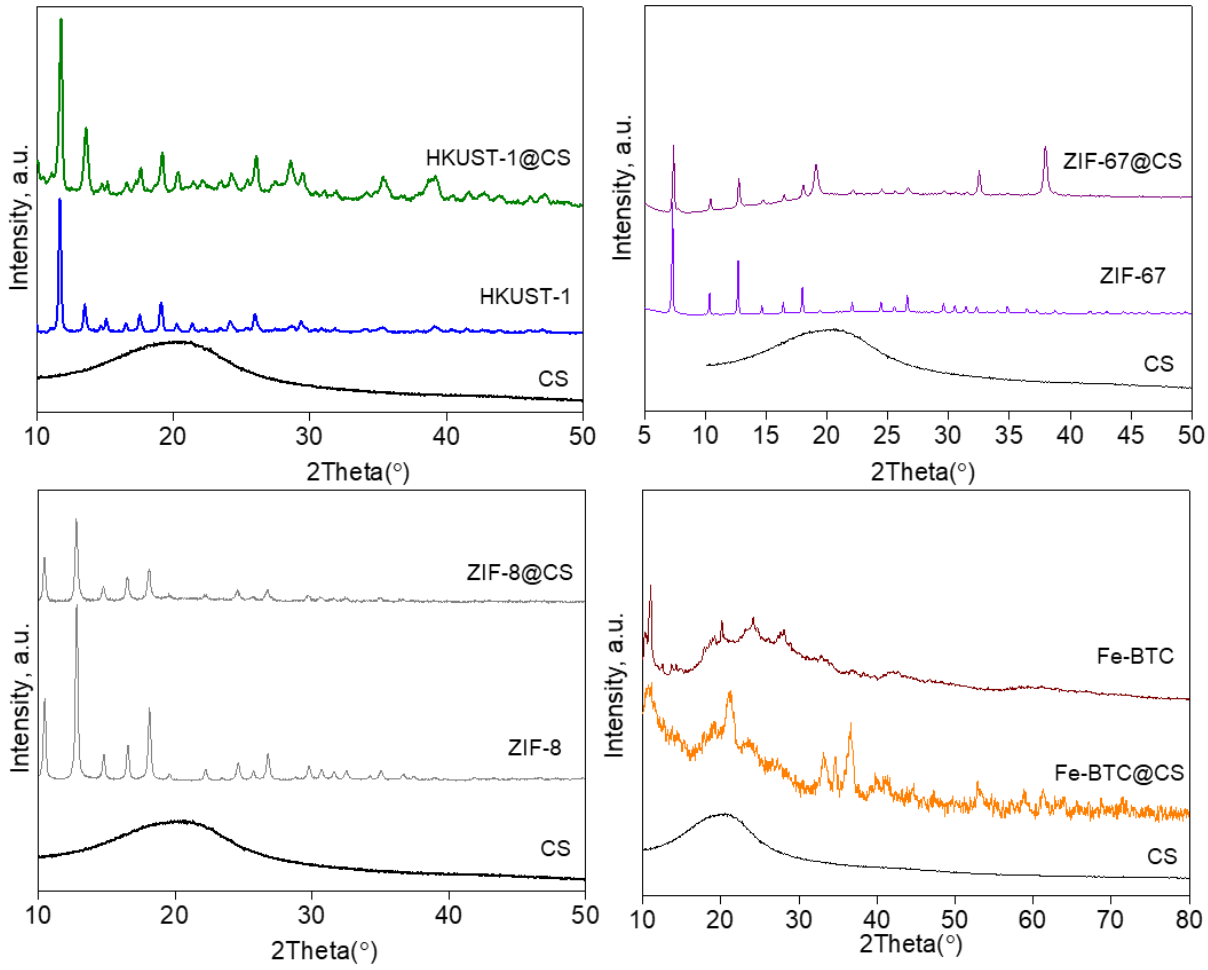


**Figure S2.** XRD patterns of MOF, chitosan and MOF-chitosan composite.

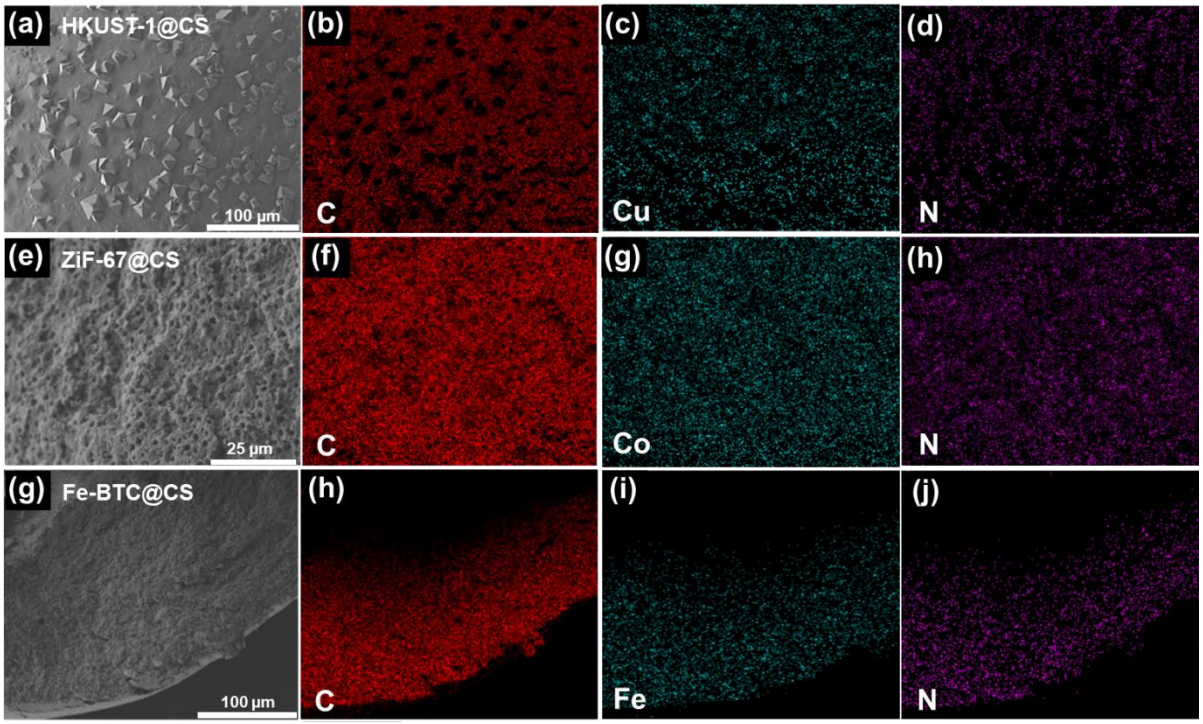


**Figure S3.** (a-d): SEM images and element mapping of **HKUST-1@CS** aerogel beads; (e-h): SEM images and element mapping of **ZiF-67@CS** aerogel beads; (g-j): SEM images and element mapping of **Fe-BTC@CS** aerogel beads.

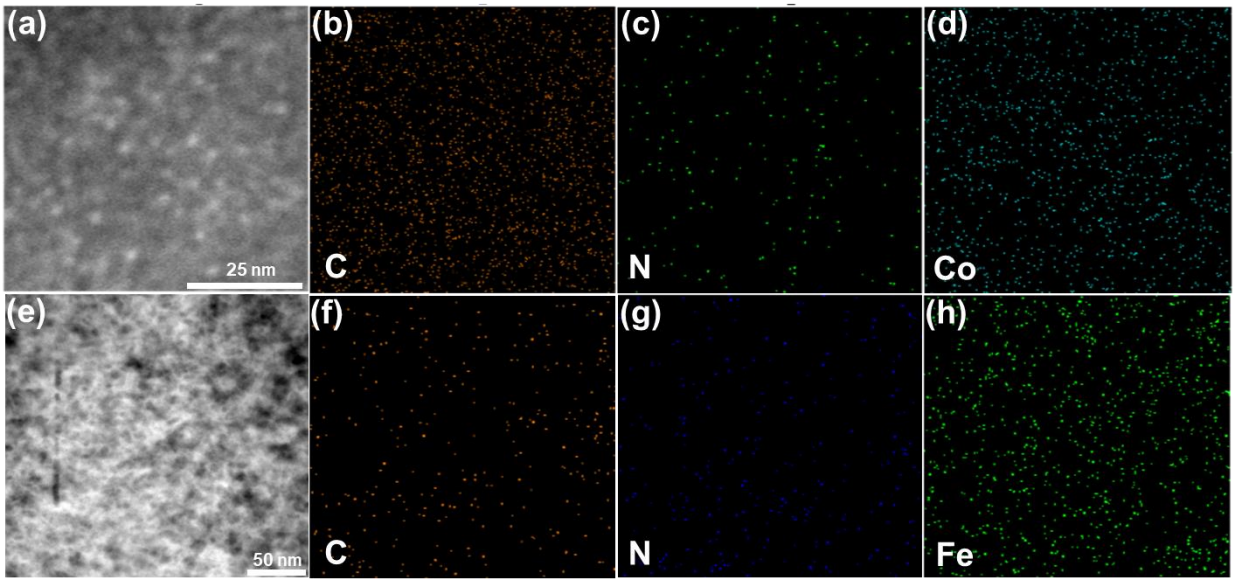


**Figure S4.** HRTEM images and element mapping of (a-d): **ZIF-67@CS** aerogel; (e-h): **Fe-BTC@CS** aerogel.

**Table S4.** Textural and structural properties of the synthesized materials.

| Samples | [a] $S_{BET}$, $m^2g^{-1}$ | [b] $S_{\mu}$, $m^2g^{-1}$ | [c] $V_p$, $cm^3g^{-1}$ | [d] $V_{\mu}$, $cm^3g^{-1}$ | [e] $D_p$, nm | Metal loading, wt.% | | | MOFs loading, wt.% | | |
|---|---|---|---|---|---|---|---|---|---|---|---|
| | | | | | | ICP | EDX | TGA | ICP | EDX | TGA |
| CS | 120 | | | | | - | - | - | - | - | - |
| Cu(MOF)@CS | 531 | 337 | 0.71 | 0.16 | 20.9 | 24 | 23 | 23 | 75 | 73 | 72 |
| Co(MOF)@CS | 283 | 47 | 0.89 | 0.01 | 21.5 | 22 | 21 | 22 | 81 | 79 | 81 |
| Zn(MOF)@CS | 232 | 101 | 0.78 | 0.05 | 18.3 | 23 | - | 23 | 81 | - | 79 |
| Fe(MOF)@CS | 163 | | 0.72 | | 20 | 17 | 16 | 16 | 81 | 76 | 76 |
| Cu(MOF)@CS_py | 141 | 8 | 1.04 | | 25.8 | - | - | - | - | - | - |
| Co(MOF)@CS_py | 257 | 78 | 0.77 | 0.02 | 24.3 | - | - | - | - | - | - |
| Zn(MOF)@CS_py | 179 | 48 | 0.81 | 0.01 | 19.4 | - | - | - | - | - | - |
| Fe(MOF)@CS_py | 121 | 1 | 0.63 | | 24.4 | - | - | - | - | - | - |

a, B.E.T. surface area; b, microporous surface area by t-plot method; c, total pore volume; d, micropore volume; e, B.J.H. mean pore size.

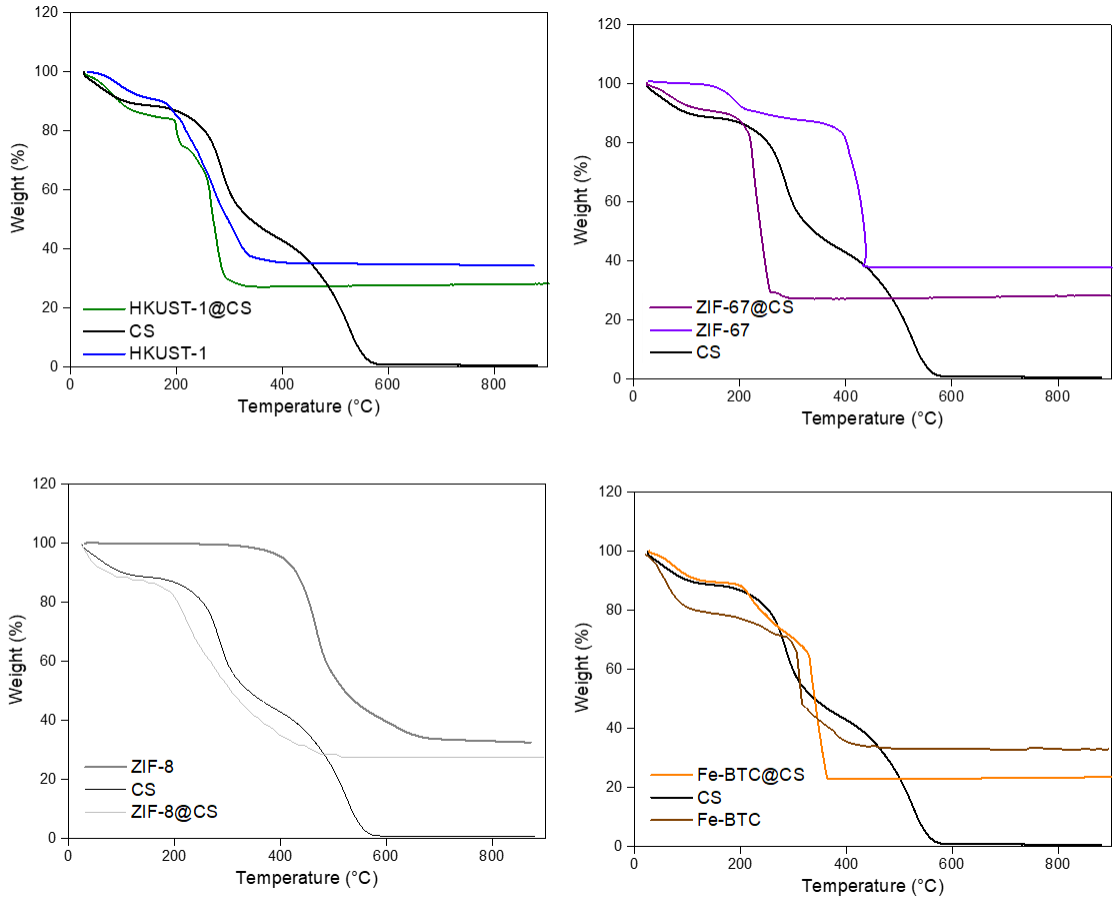


**Figure S5.** TGA curves of **HKUST-1@CS, ZIF-67@CS, Fe-BTC@CS** and **ZIF-8@CS.**

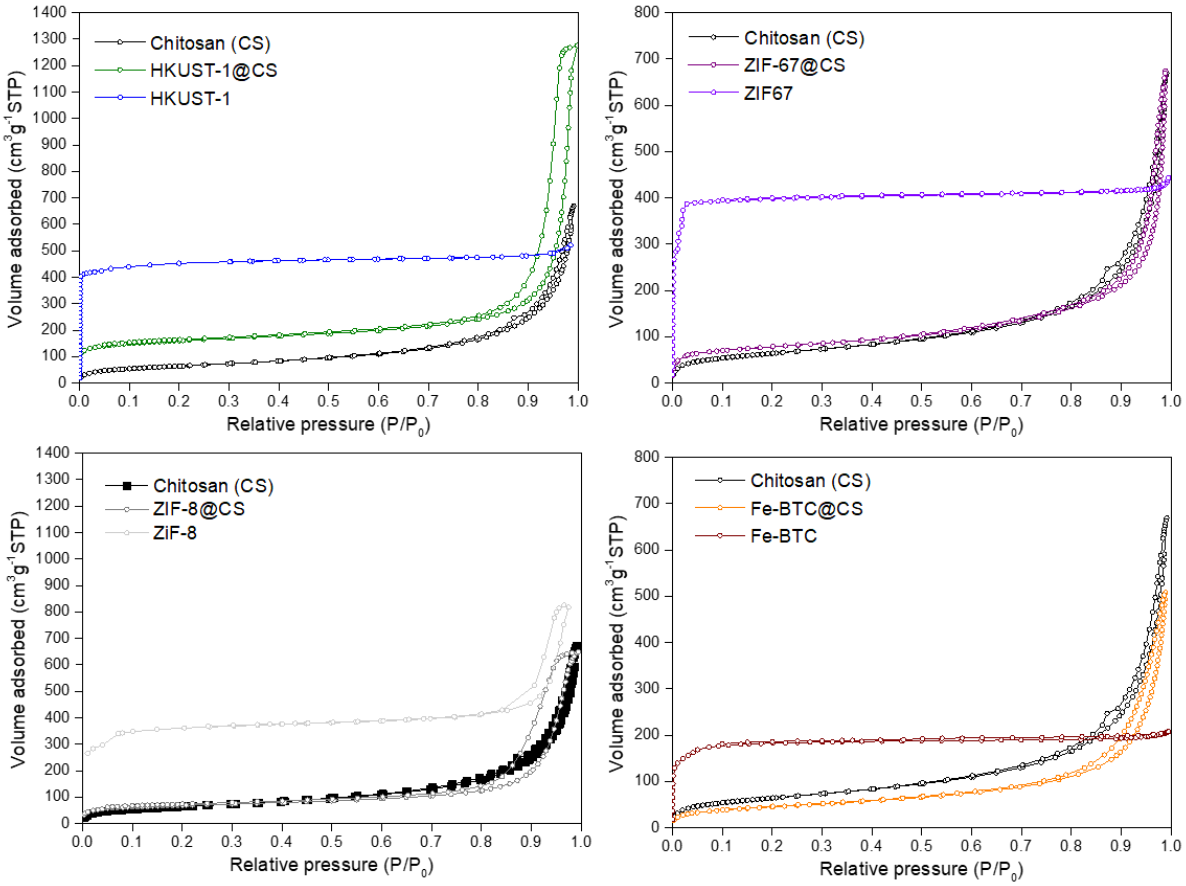


**Figure S6.** $N_2$-physisorption isotherms obtained for **HKUST-1@CS**, **ZIF-67@CS**, **Fe-BTC@CS** and **ZIF-8@CS**.

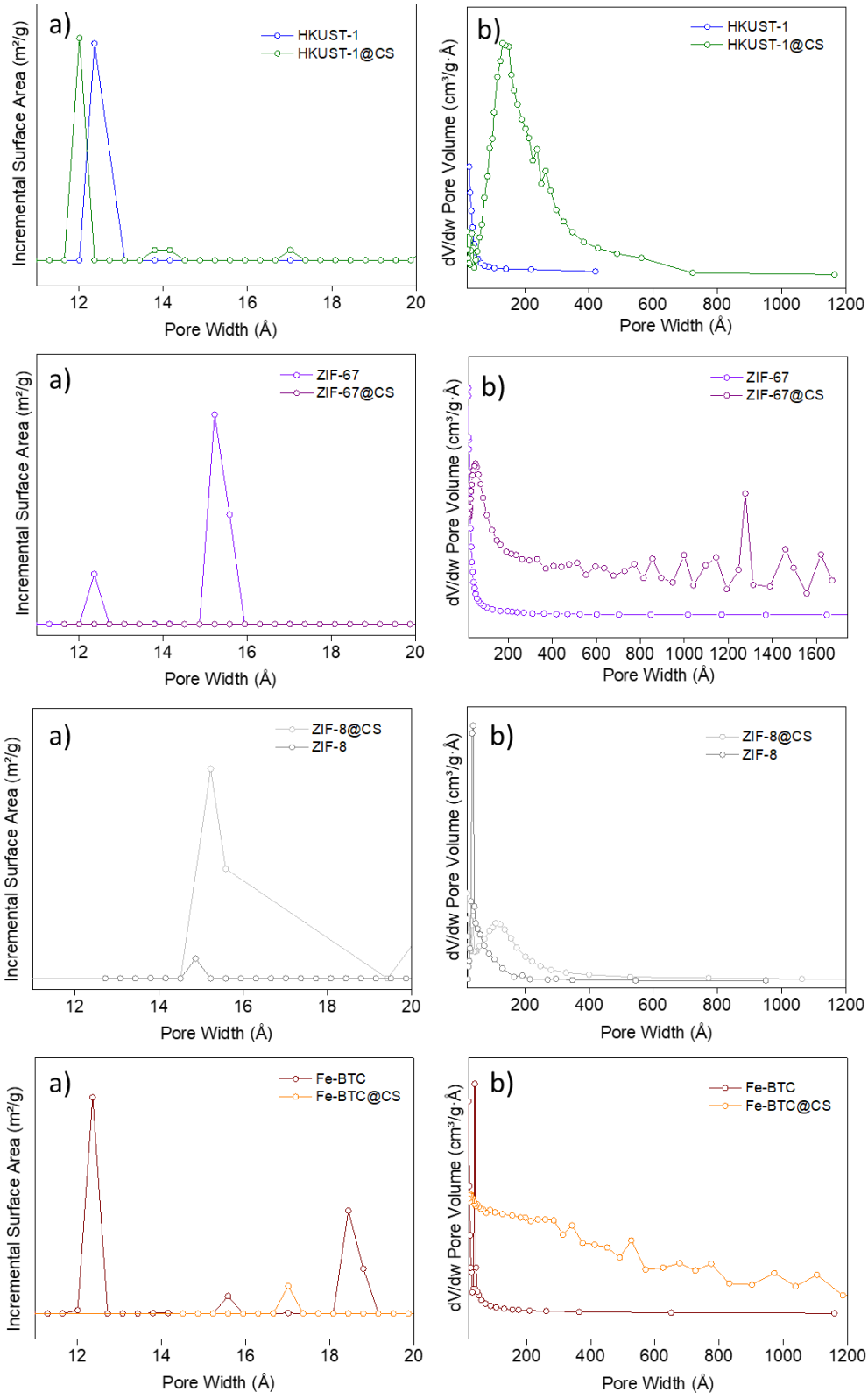


**Figure S7**. (a) Non local density functional theory (NLDFT) pore size distribution plots in the micropore range; (b) Barrett–Joyner–Halenda (BJH) adsorption pore size distributions for **HKUST-1@CS**, **ZIF-67@CS**, **Fe-BTC@CS** and **ZIF-8@CS**.

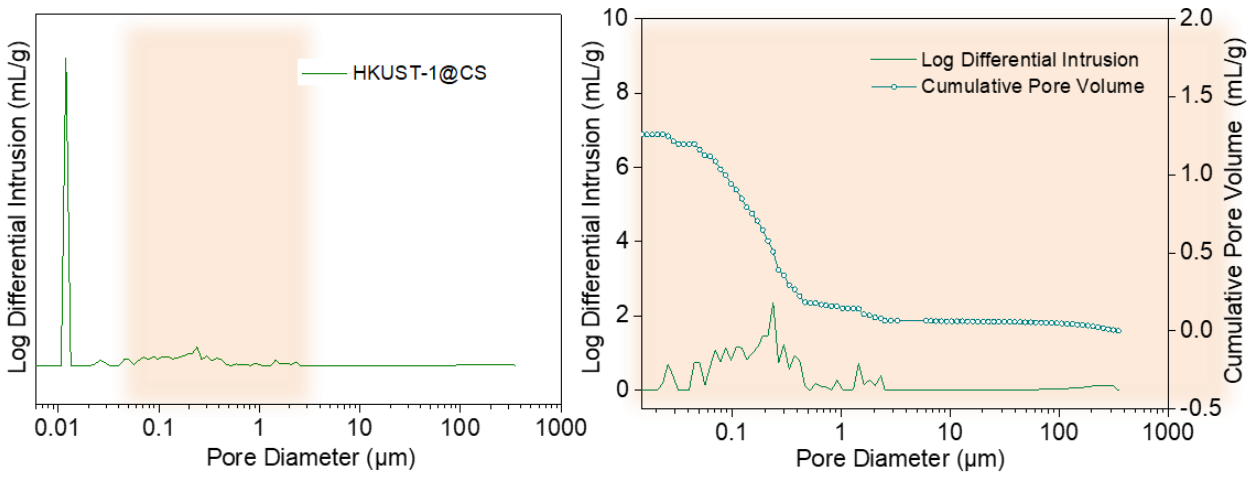


**Figure S8**. Differential and cumulative intrusions versus pore diameter of **HKUST-1@CS** based on mercury intrusion porosimetry.

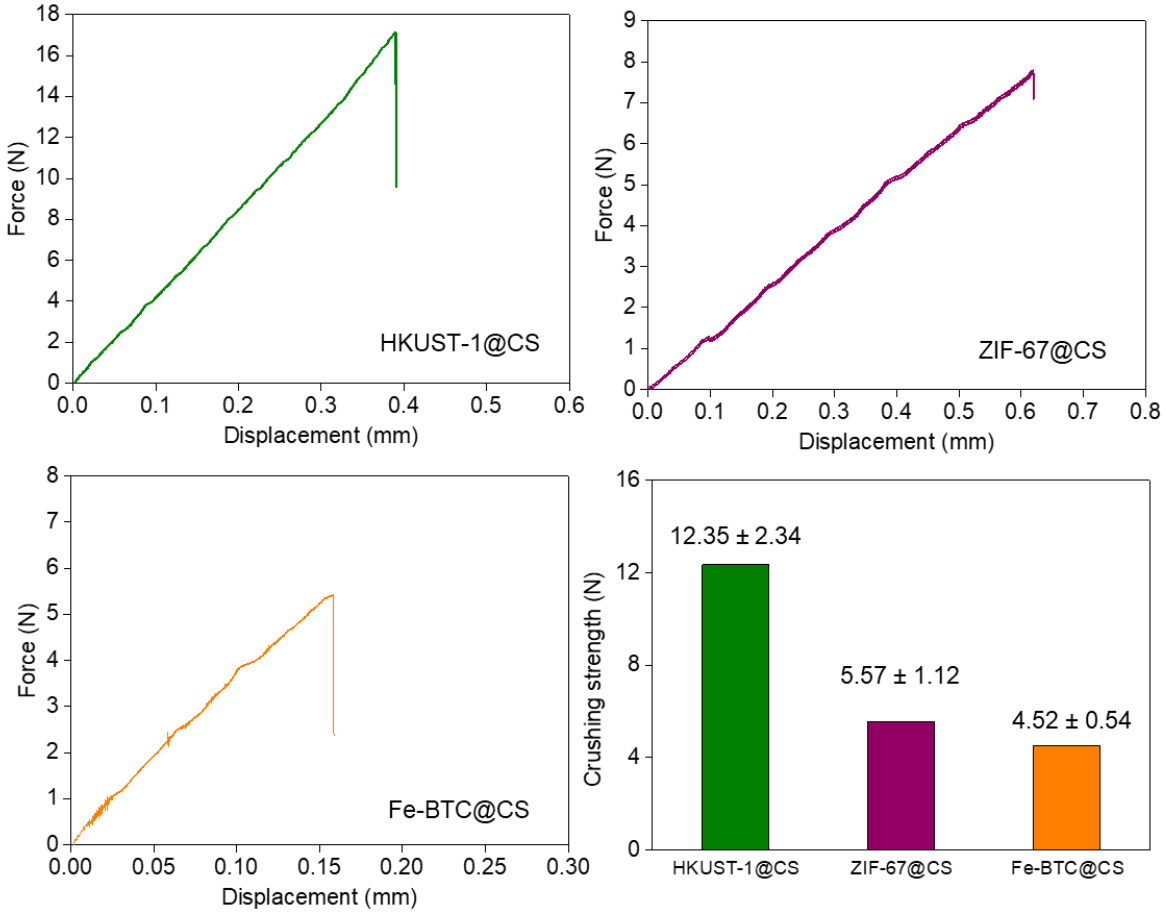


**Figure S9**. Force- displacement curves obtained via crush testing (a), and average crushing strength (b), of **HKUST-1@CS**, **ZIF-67@C** and **Fe-BTC@CS** .

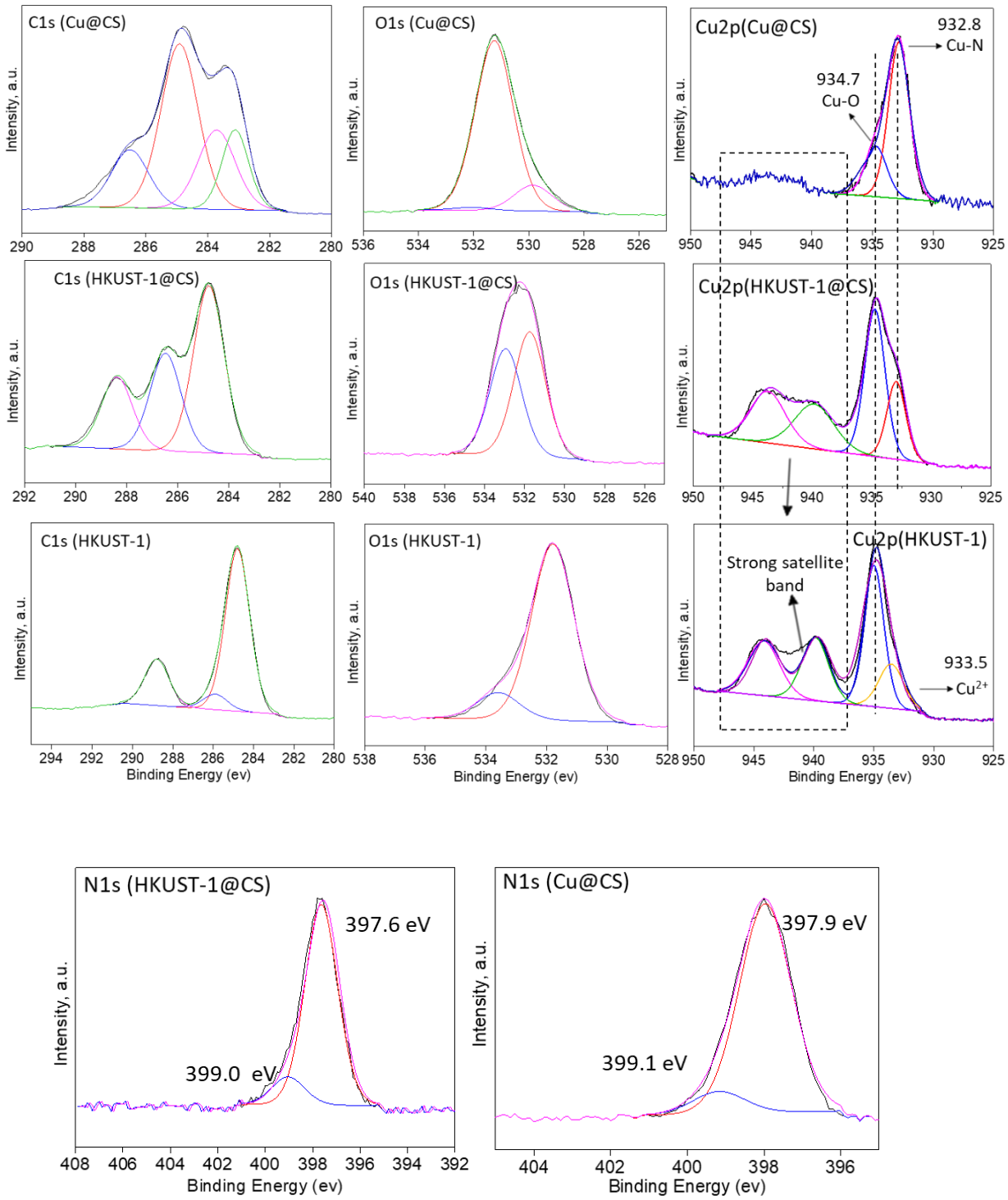


**Figure S10.** High -resolution XPS spectra of C (1s), N(1s) and O(1s) of the HKUST-1, Cu@CS and **HKUST-1@CS** aerogels.

**Table S5.** Elemental compositions and O/N ratio of the HKUST-1, Cu@CS and HKUST-1@CS aerogels.

| | Atomic concentration (%) | | | | O/N ratio |
|---|---|---|---|---|---|
| | C (1s) | O (1s) | N (1s) | Cu (2p) | |
| HKUST-1 | 67.0 | 28.3 | - | 4.7 | - |
| Cu@CS | 69.0 | 25.0 | 5.5 | 3.1 | 4.5 |
| HKUST-1@CS | 64.1 | 29.2 | 3.4 | 3.3 | 8.5 |

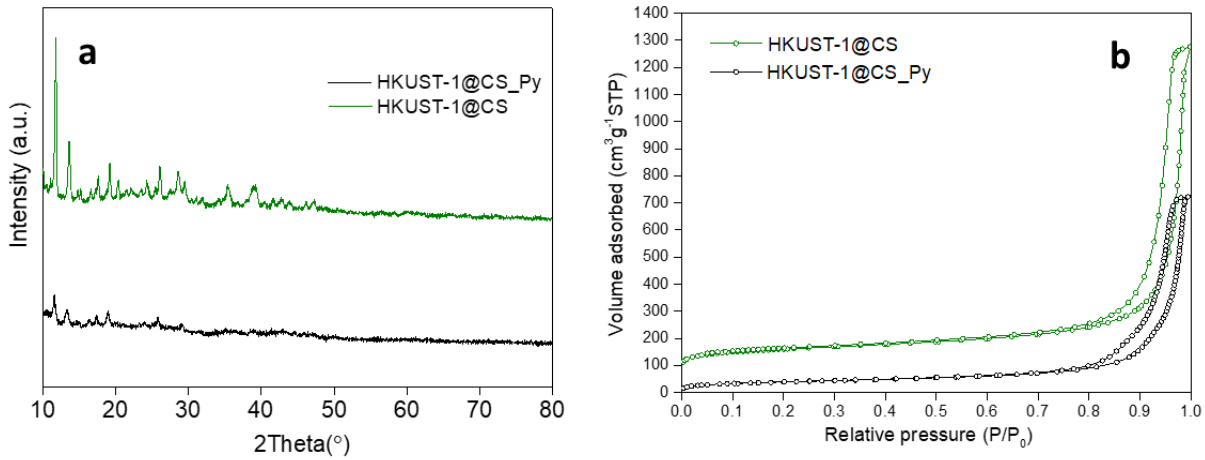


**Figure S11.** XRD patterns (a) and $N_2$-Adsorption desorption (b) of **HKUST-1@CS** before and after pyrolysis.

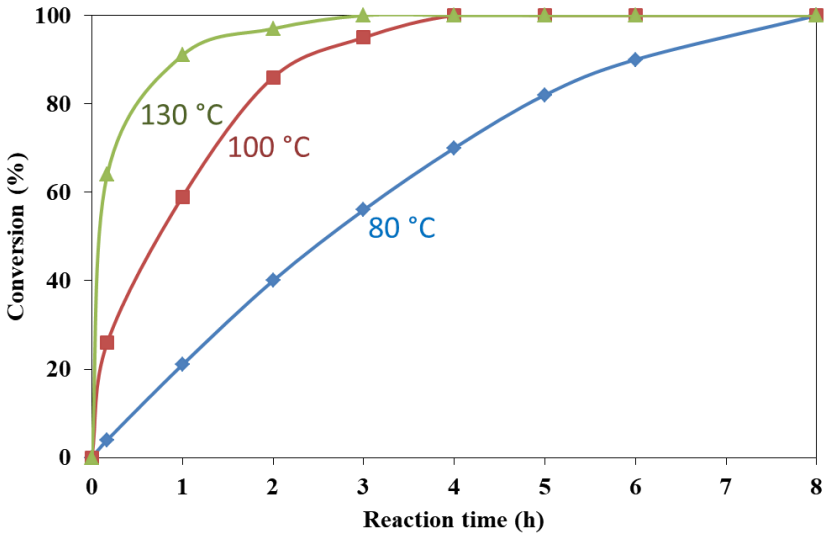


**Figure S12.** Time-yield plots for the oxidation of 1 to 2 over **HKUST-1@CS** aerogel at different reaction temperatures (i.e., 80 °C, 100 °C, 130 °C), other reaction condition: 0.8 mmol reactant, 1 mL ethanol/water (1/1, v/v), catalyst/reactant solution ratio 8 wt.%, 5 bar $O_2$.

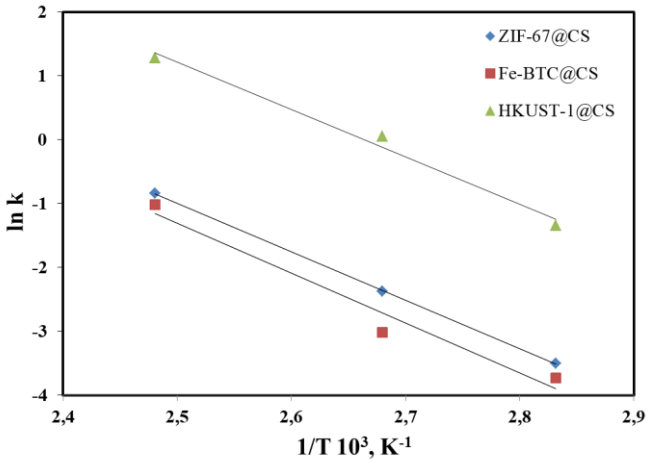


**Figure S13.** Arrhenius plot correlating the inverse of the absolute temperature with the rate constant in the presence of **HKUST-1@CS**, **ZIF-67@CS** and **Fe-BTC@CS**.

The activation energies were obtained from the slope of the best fitting of the experimental points to a straight line and applying the Arrhenius equation [Ln(k) = -Ea/RT +Ln(A)]. The experimental equations for the three catalysts were: $Ln(k_{Cu)} = -7.4*(1/T) + 19.8$; $Ln(k_{Co)} = -7.6*(1/T) + 18.0$; $Ln(k_{Fe)} = -7.8*(1/T) + 18.3$.

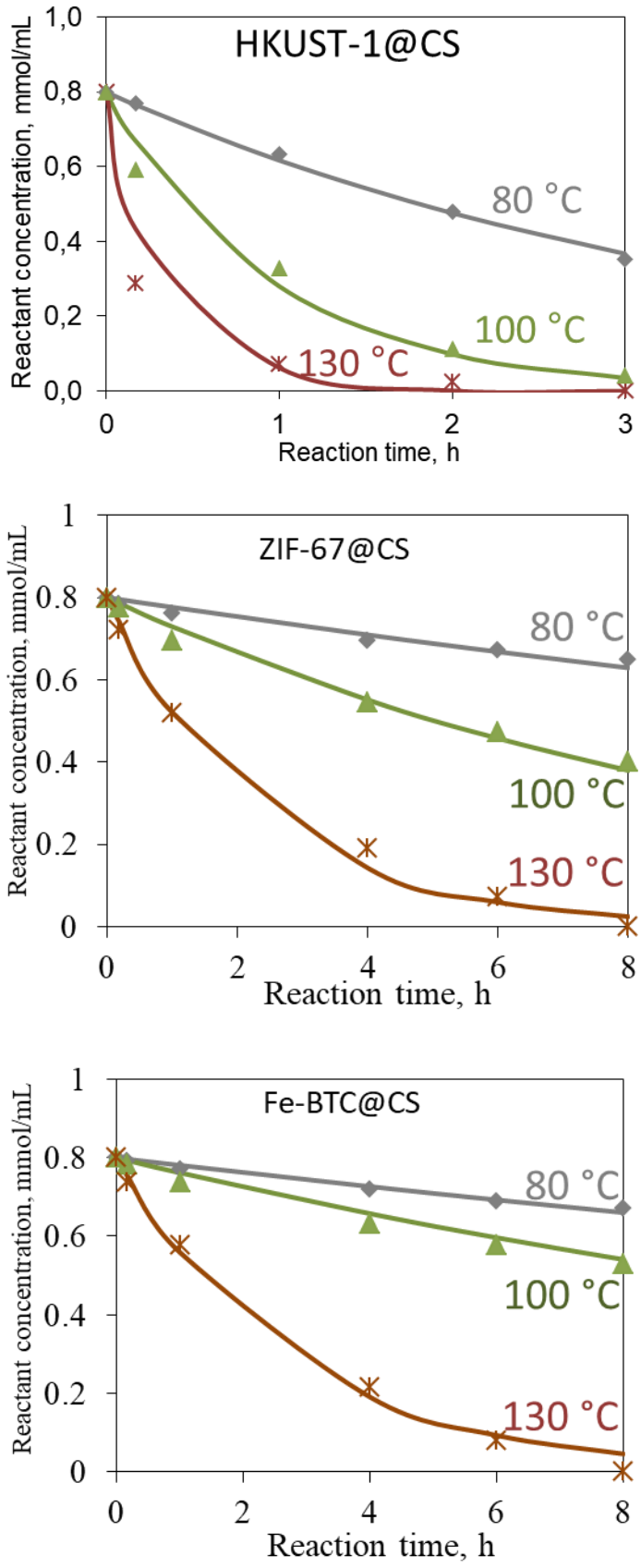


**Figure S14.** Simulated kinetic patterns of cyclohexane oxime 1 conversion using first order kinetic for HKUST-1@CS, ZIF-67@CS and Fe-BTC@CS at 80 °C, 100 °C and 130 °C. The solid lines in each figure represent the simulation data. The data points in

each figure represent the experimental data. Reaction conditions: 0.8 mmol reactant, 1 mL ethanol/water (1/1, v/v), catalyst/reactant solution ratio 8 wt.%, 5 bar $O_2$.

**Table S6**. Constant rates (k) at different reaction temperatures for **HKUST-1@CS, ZIF-67@CS** and **Fe-BTC@CS** for the oxidative conversion of cyclohexane oxime 1 to cyclohexanone 2.

| Reaction T, °C | HKUST-1@CS | ZIF-67@CS | Fe-BTC@CS |
|---|---|---|---|
| 80 | 0.26 | 0.03 | 0.02 |
| 100 | 1.05 | 0.09 | 0.05 |
| 130 | 4.0 | 0.43 | 0.36 |

**Table S7**. Comparison of catalytic performances of reported catalysts in literature for cyclohexanone oxime oxidation

| Entry | Catalyst | T, °C | P($O_2$), bar | TON[a] ( time, h) | TOF, [b] $h^{-1}$ | Ref |
|---|---|---|---|---|---|---|
| 1 | Au (0.72 wt.%)/$CeO_2$ | 100 | 5 | 6800 (1) | 6800 | [1] |
| 2 | $NaNO_2$ | 25 | 1 | 8.2 (6) | 1.4 | [2] |
| 3 | $Ce(SO_4)_2$ | 25 | - | 0.2 (2) | 0.1 | [3] |
| 4 | $SnCl_2$ and $TiCl_3$ | 25 | - | 0.3 (3) | 0.1 | [4] |
| 5 | $Cu_3[Co(CN)_6]_2$ | 100 | 5 | 6.3 (1) | 6.3 | [5] |
| 6 | ZIF-67@CS | 100 | 5 | 35.9 (6) | 6.0 | This work |
| 7 | ZIF8@CS | 100 | 5 | 1.4 (6) | 0.2 | This work |
| 8 | Fe-BTC@CS | 100 | 5 | 21.6 (6) | 3.6 | This work |
| 9 | HKUST-1@CS | 100 | 5 | 13.0 (1) | 13.0 | This work |


[1] A. Grirrane, A. Corma and H. Garcia, *J. Catal.*, 2009, **268**, 350–355.

[2] G. Zhang, X. Wen, Y. Wang, W. Mo and C. Ding, J. Org. Chem., 2011, **76**, 4665–4668.

[3] O. Asutay, N. Hamarat, N. Uludag, N. Coşkun, Tetrahedron Lett., 2015, **56**, 3902-3904.

[4] M.-H. Lin, H.-J. Liu, C.-Y. Chang, W.-C. Lin, T.-H. Chuang, Molecules , 2012, **17,** 2464-2473.

[5] A. García-Ortiz, A. Grirrane, E. Reguera, H. García, *J. Catal.*, 2014, **311**, 386-392.

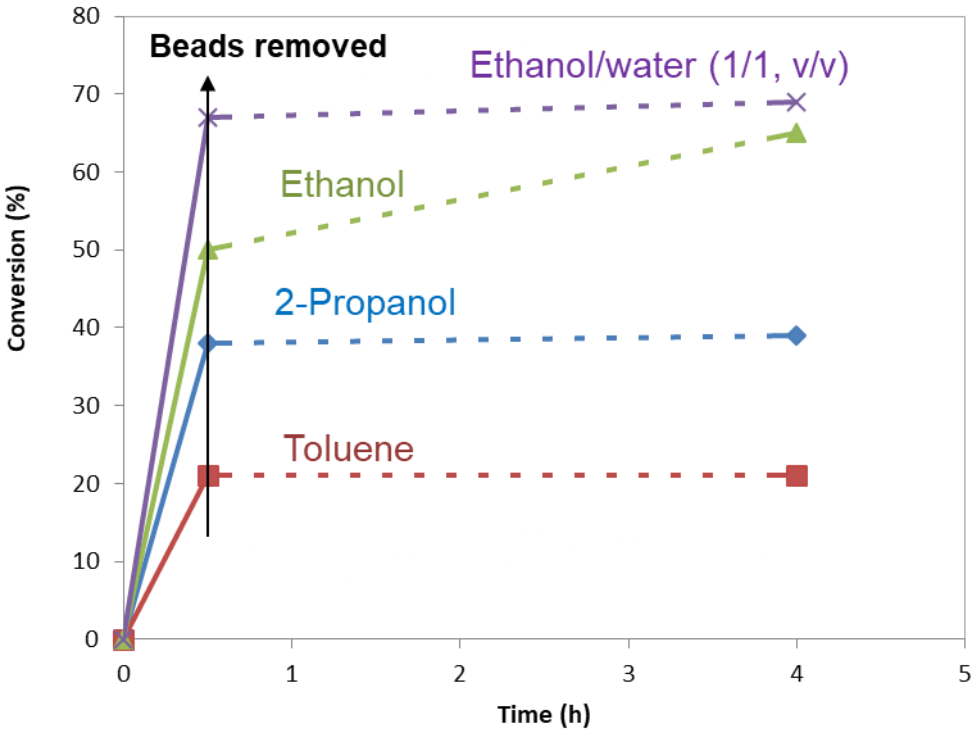


**Figure S15.** Hot filtration test of HKUST-1@CS in different reaction medium, reaction conditions: 0.8 mmol reactant, 1 mL ethanol/water (1/1, v/v), catalyst/reactant solution ratio 8 wt.%, 80 °C, 5 bar $O_2$. The catalyst was filtered out at the reaction time of 0.5 h.

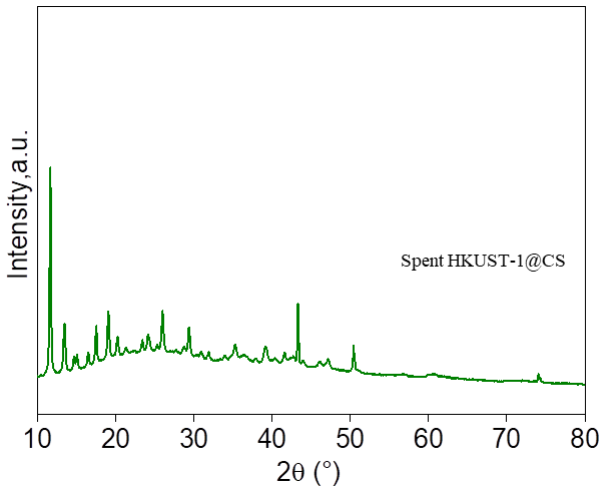

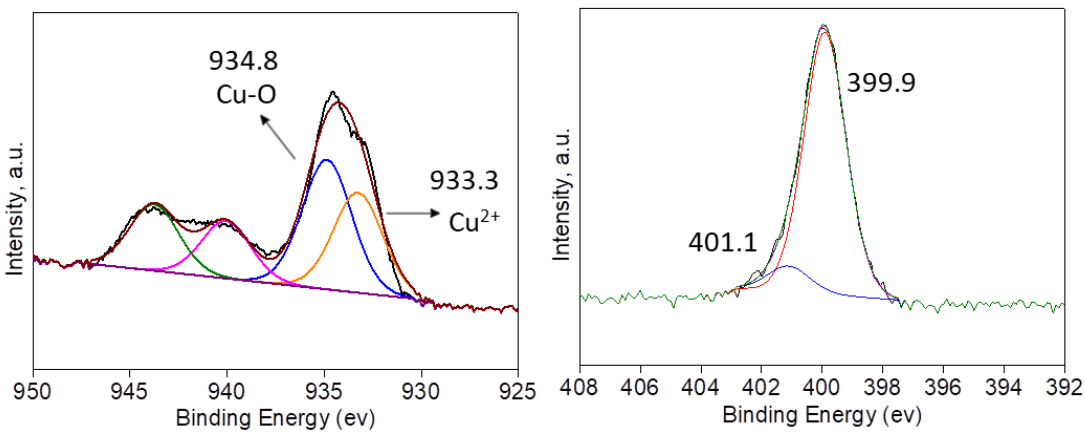


**Figure S16.** XRD pattern and XPS spectra of the spent HKUST-1@CS catalyst.

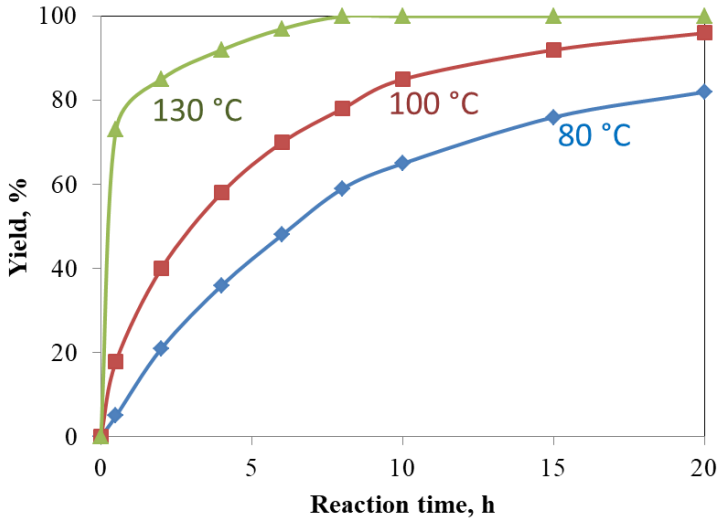


**Figure S17.** Time-yield plots for the oxidation of 5 (carvone oxime) in the presence of HKUST-1@CS at different reaction temperatures (i.e., 80 °C, 100 °C, 130 °C). Reaction conditions: 0.8 mmol reactant, 1 mL ethanol/water (1/1, v/v), catalyst/reactant solution ratio 8 wt.%, 5 bar $O_2$.

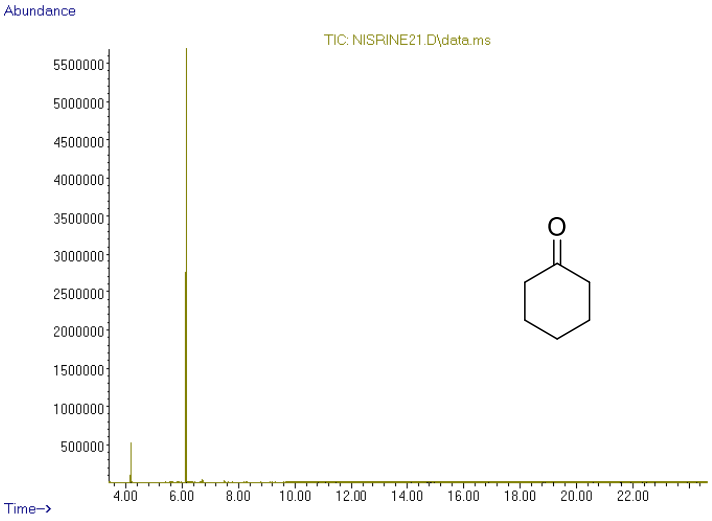
Abundance
TIC: NISRINE21.D\data.ms
5500000
5000000
4500000
4000000
3500000
3000000
2500000
2000000
1500000
1000000
500000
4.00
6.00
8.00
10.00
12.00
14.00
16.00
18.00
20.00
22.00
Time-->

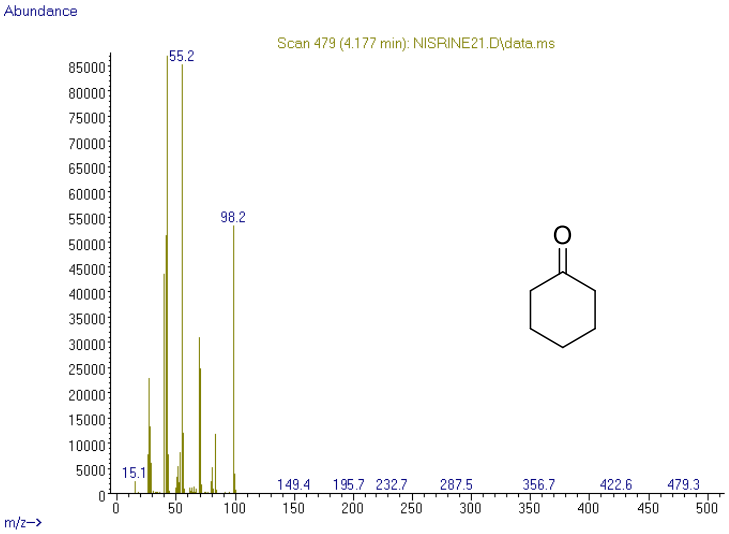
Abundance
Scan 479 (4.177 min): NISRINE21.D\data.ms
55.2
98.2
85000
80000
75000
70000
65000
60000
55000
50000
45000
40000
35000
30000
25000
20000
15000
10000
5000
0
15.1
149.4
195.7
232.7
287.5
356.7
422.6
479.3
0
50
100
150
200
250
300
350
400
450
500
m/z-->

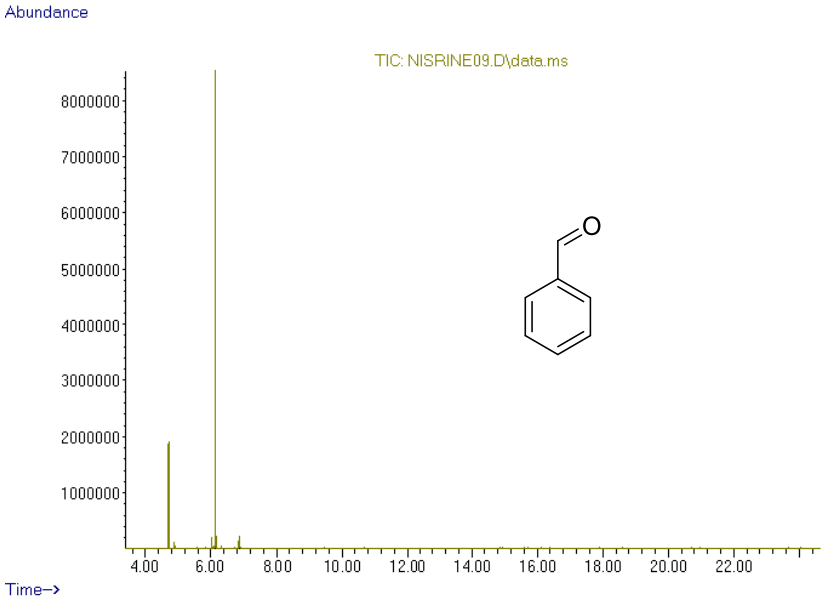
Abundance
TIC: NISRINE09.D\data.ms
8000000
7000000
6000000
5000000
4000000
3000000
2000000
1000000
4.00
6.00
8.00
10.00
12.00
14.00
16.00
18.00
20.00
22.00
Time-->

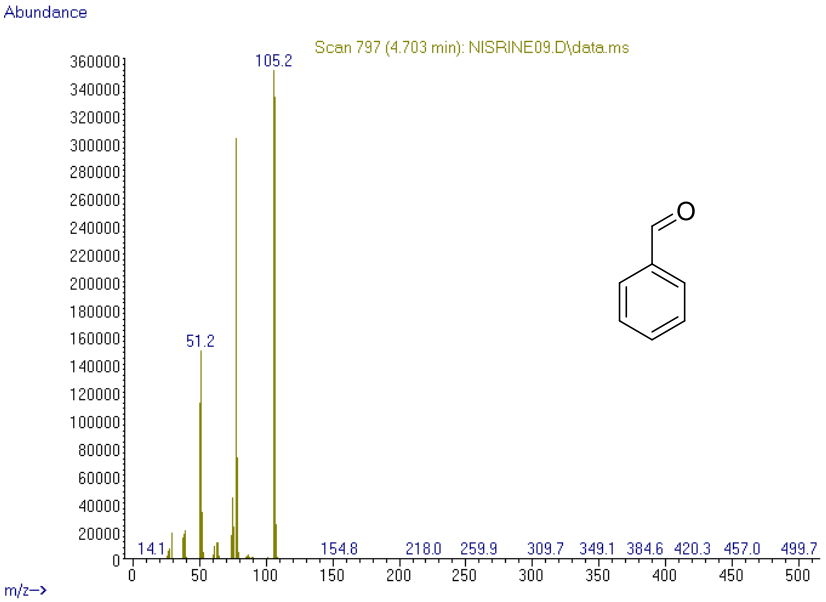
Abundance
Scan 797 (4.703 min): NISRINE09.D\data.ms
105.2
51.2
14.1
154.8
218.0
259.9
309.7
349.1
384.6
420.3
457.0
499.7
m/z-->

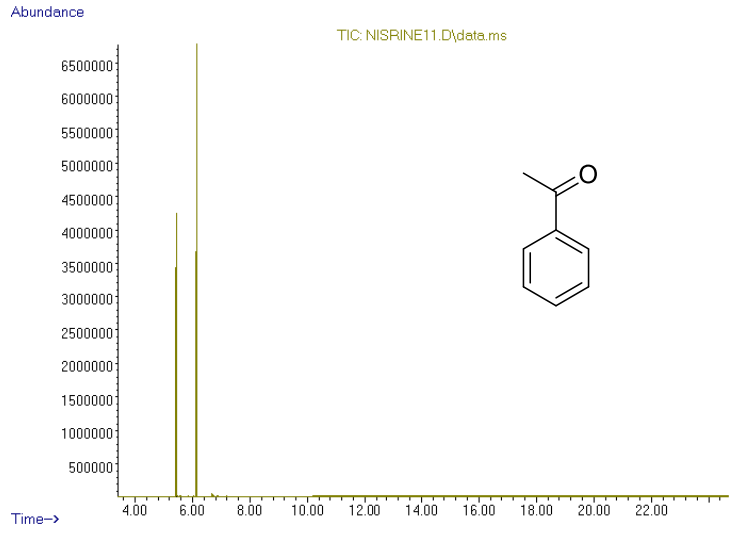
Abundance
TIC: NISRINE11.D\data.ms
Time-->

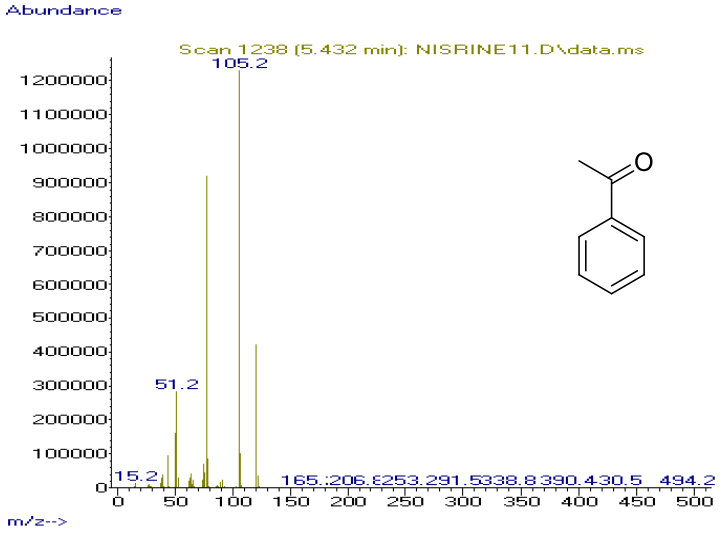
Abundance
Scan 1238 (5.432 min): NISRINE11.D\data.ms
105.2
51.2
15.2
165.2
206.2
253.2
291.5
338.8
390.4
430.5
494.2
m/z-->

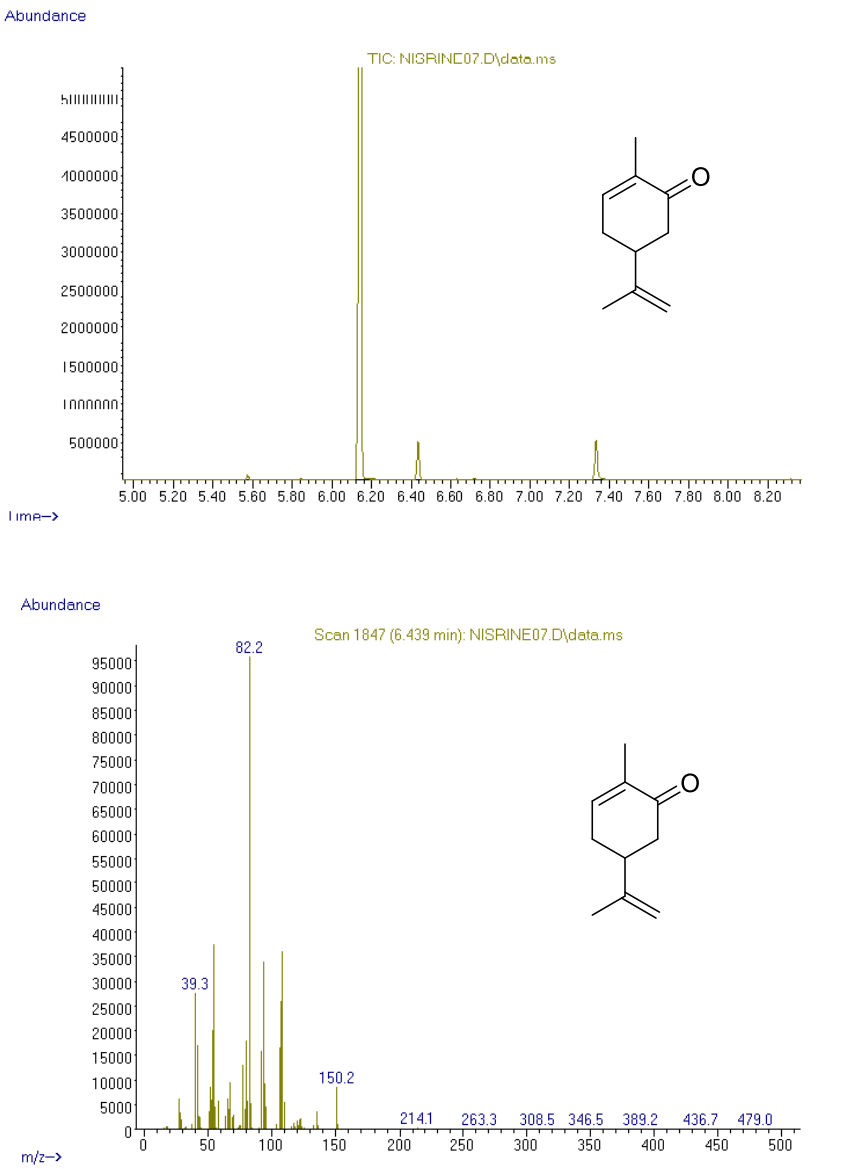


**Figure S18.** GC_MS spectrum of products analysis.

**$^{1}$H NMR** (300 MHz, Methylene Chloride-$d_2$) δ 10.05 (s, $H_8$, 1H), 8.00 – 7.80 (m, $H_1$+$H_3$, 2H), 7.74 – 7.65 (m, $H_5$, 1H), 7.63 – 7.53 (m, $H_4$+$H_6$, 2H).

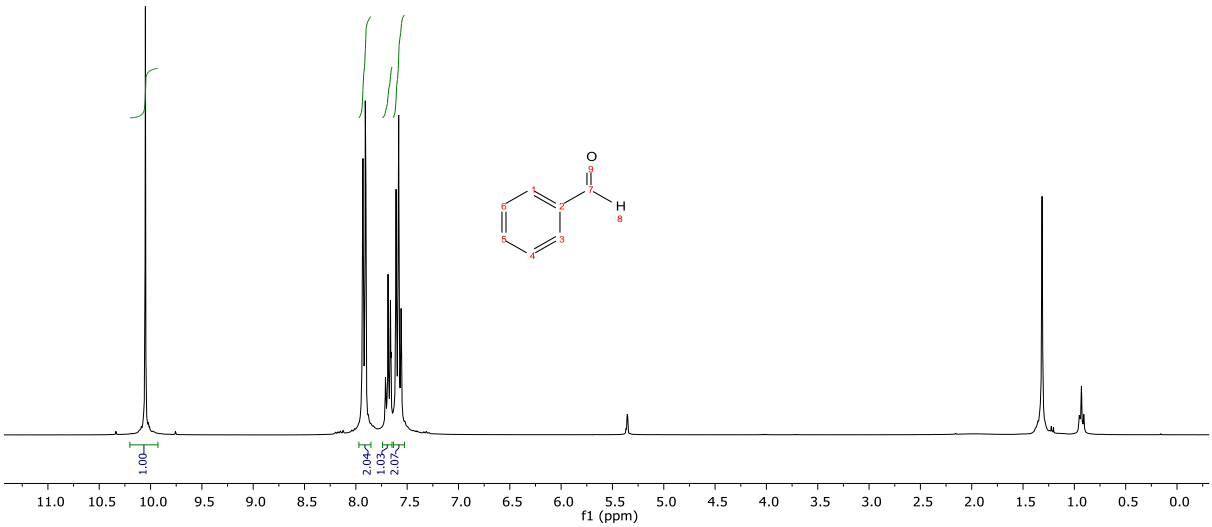


**$^{13}$C NMR** (75 MHz, $CD_2Cl_2$) δ 192.69 (C7), 136.94 (C2), 134.78 (C5), 129.98 (C1+C3), 129.39 (C4+C6).

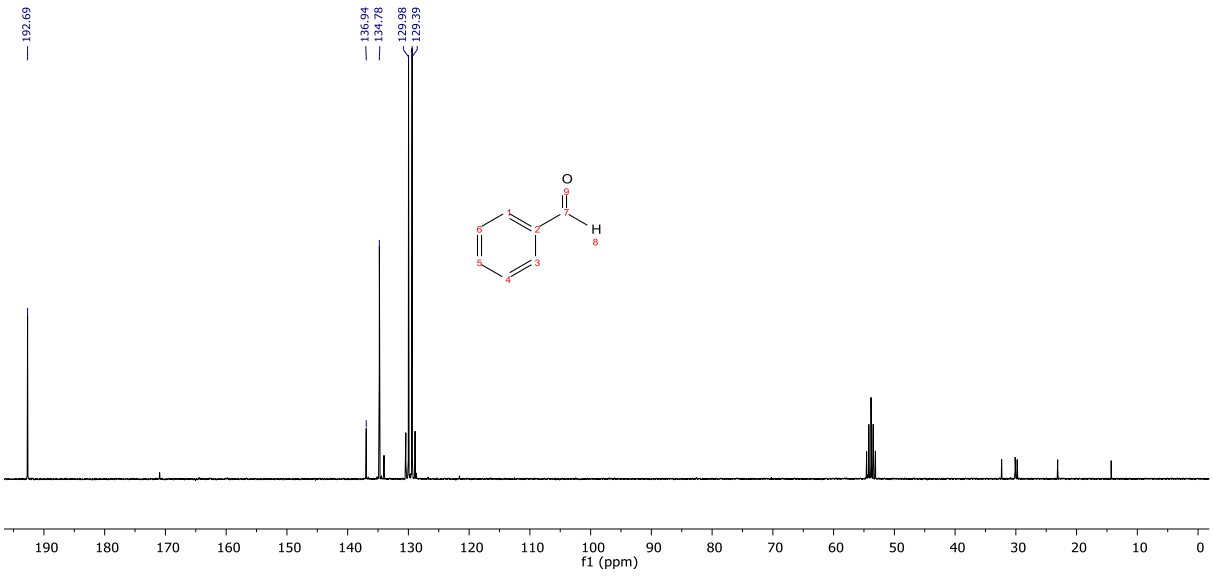

## Cyclohexanone

**$^{1}$H NMR** (300 MHz, Methylene Chloride-$d_2$) δ 2.31 (m, $H_2$+$H_6$, 1H), 1.94 – 1.80 (m, $H_5$+$H_3$,1H), 1.72 (m, $H_4$, 1H).

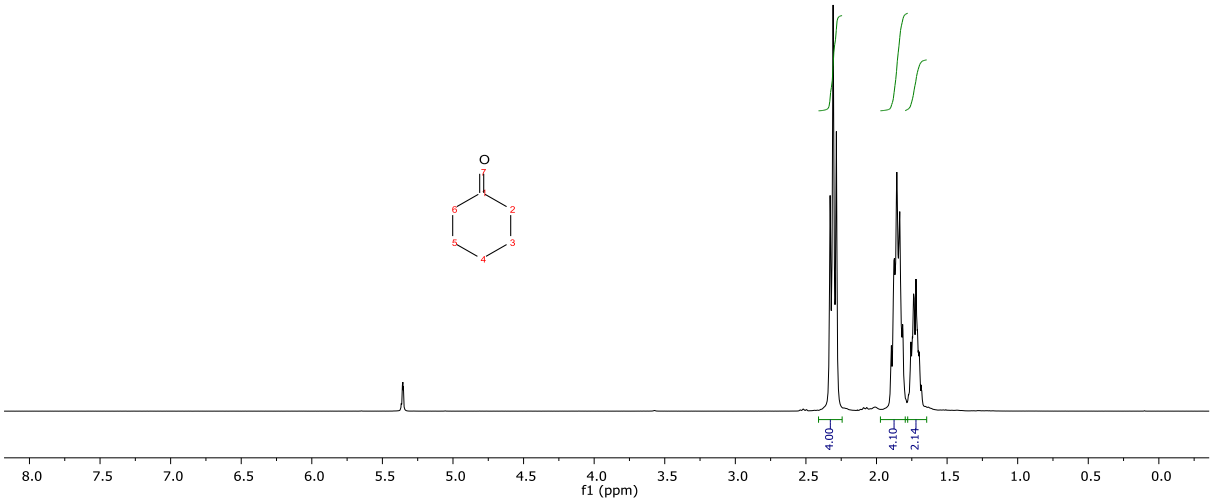


**$^{13}$C NMR** (75 MHz, $CD_2Cl_2$) δ 211.56 (C1), 42.24 (C2+C6), 27.41 (C3+C5), 25.36 (C4).

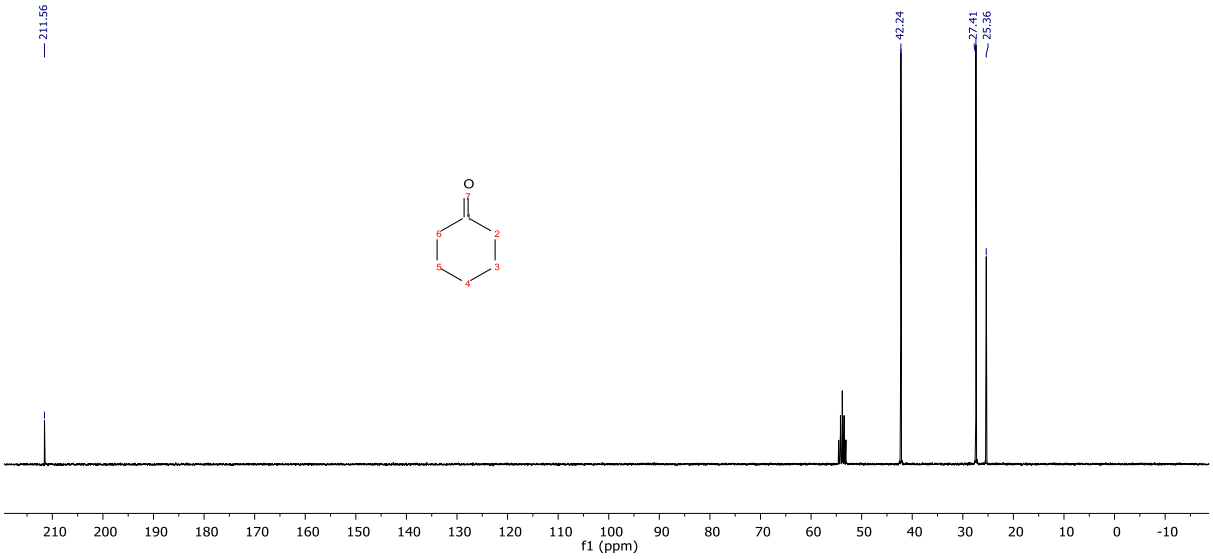


## Carvone

**$^{1}$H NMR** (300 MHz, Methylene Chloride-$d_2$) δ 6.78 (ddq, $J$ = 5.9, 3.3, 1.6 Hz, $H_6$, 1H), 4.91 – 4.72 (m, $H_{10}$, 2H), 2.71 (m, $H_4$, 1H), 2.61 – 2.20 (m, $H_3$+$H_5$, 4H), 1.78 (s, $H_8$+$H_{11}$, 6H).

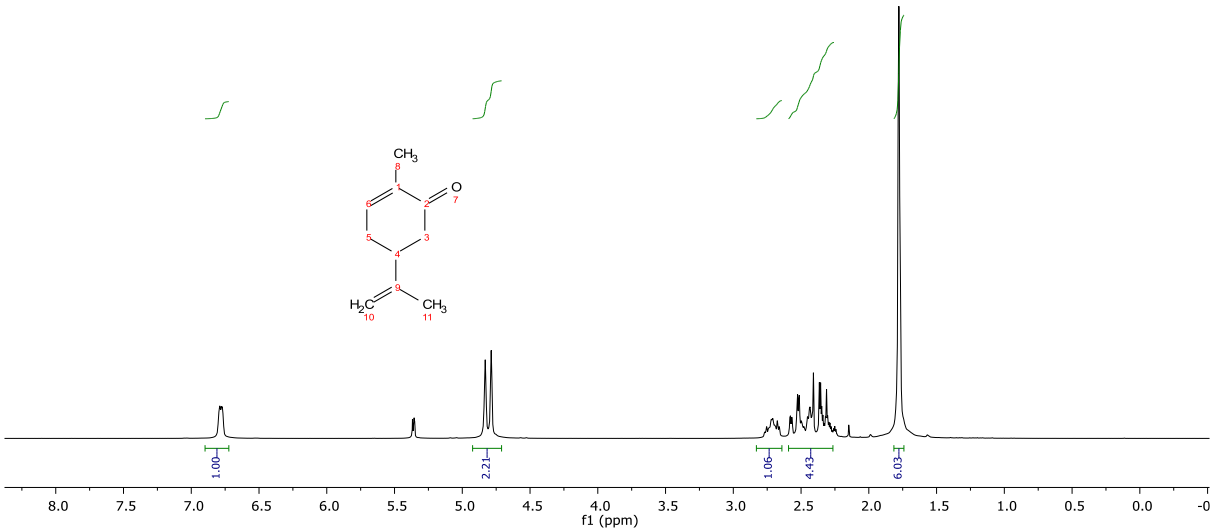


**$^{13}$C NMR** (75 MHz, $CD_2Cl_2$) δ 199.58 (C2), 147.53 (C7), 144.80 (C5), 135.55 (C1), 110.36 (C10), 43.51 (C3), 42.91 (C4), 31.62 (C5), 20.60 (C11), 15.76 (C8),

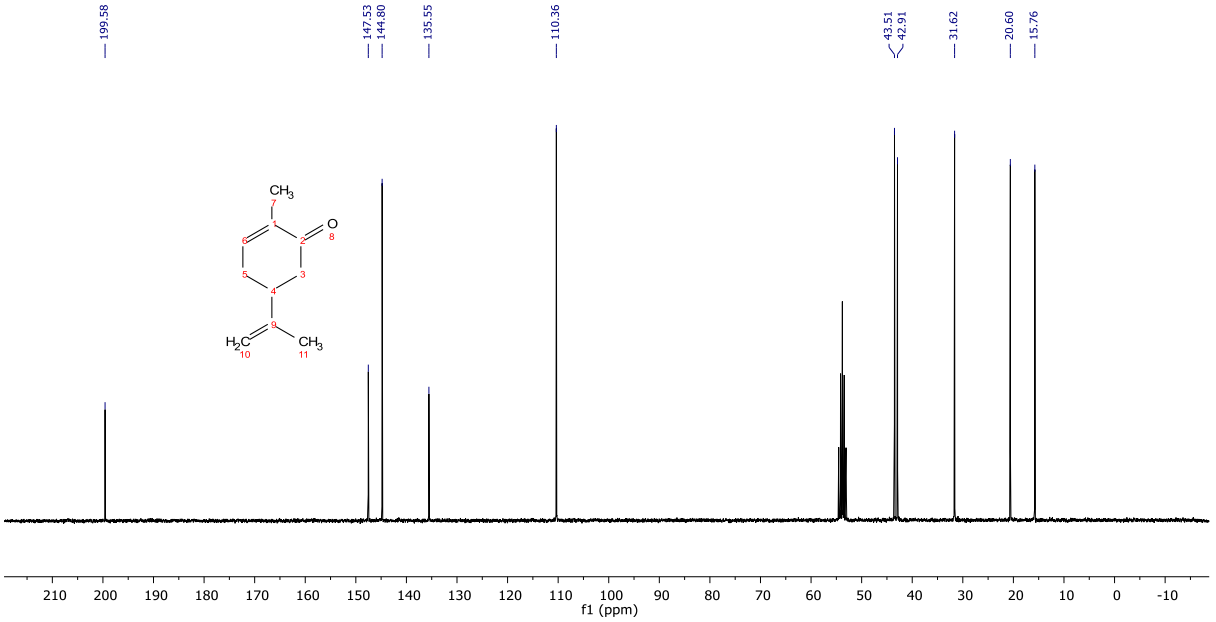


**Figure S19.** NMR data of products analysis.